Proceedings of the ASME Turbo Expo 2023
Turbomachinery Technical Conference and Exposition
GT2023
June 26-30, 2023, Boston, Massachusetts

GT2023-102042

ROLE OF TURBULENCE IN MODIFYING THE COHERENT HEAT RELEASE RESPONSE OF ACOUSTICALLY EXCITED ROD-STABILIZED FLAMES

Ashwini Karmarkar*and Jacqueline O'Connor
Department of Mechanical Engineering
Pennsylvania State University
University Park, Pennsylvania 16802

ABSTRACT

Modern power generation gas turbine engines operate in primarily fuel-lean conditions in order to mitigate harmful emissions. Lean combustion systems, however, are susceptible to combustion instabilities, which arise from a resonant coupling between coherent oscillations in the unsteady heat release rate and the acoustic modes of the combustor. The occurrence of combustion instabilities can severely limit engine performance and operability. To design effective instability control mechanisms, it is critical to understand the response of flames to coherent fluctuations in the velocity and pressure fields of the flow. In addition to coherent oscillations, combustor flow fields also experience high levels of perturbations arising from turbulence, which can significantly alter the flow and flame dynamics. In this work, we study the coherent heat release response of a rod-stabilized flame subjected to longitudinal acoustic forcing at two levels of in-flow turbulence. We systematically vary the amplitude of acoustic excitation at two frequencies - the natural frequency of vortex shedding and its first harmonic – at both turbulence levels. Our results show that the amplitude of the coherent heat release response is strongly dependent on the turbulence intensity. Additionally, the impact of turbulence on the coherent heat release response is a function of the acoustic forcing frequency. These results provide insight into the interaction between coherent and turbulent motions in the flow and their impact on unsteady heat release oscillations in gas turbine combustors.

NOMENCLATURE

A Disturbance amplitude
B Disturbance decay rate
C Ratio of disturbance spatial wavelengths
K Propagation speed ratio
S Total flame disturbance
S_T Turbulent flame speed
V_{pp} Forcing voltage
$\tilde{c}$ Flame progress variable
f_0 Forcing frequency
f_s Sampling frequency
k Wavenumber
l_f Flame length
n Non-local disturbance amplitude
$\tilde{p}$ Coherent pressure fluctuation
s Individual flame disturbance waveform
t Time
u' Turbulent fluctuation
$\bar{u}$ Time-averaged velocity
u_c Convection velocity
w_f Flame wrinkle amplitude
x Downstream coordinate
y Cross-stream coordinate
$\tilde{\Phi}$ Global coherent chemiluminescence fluctuation
$\tilde{\Psi}$ Local coherent chemiluminescence fluctuation
α Disturbance decay rate
$\Delta\phi$ Phase delay
ω Angular frequency

*Address all correspondence to this author. Author's new affiliation: Argonne National Laboratory, akarmarkar@anl.gov

$\tilde{\omega}$ Coherent vorticity fluctuation

INTRODUCTION

Bluff-body stabilized flames are used in a number of gas turbine combustion applications, including both main combustors and afterburners [1]. Flame stabilization is greatly enhanced through the use of bluff bodies, as the recirculation zone downstream of the bluff body provides a region of hot, radical-filled gases to back-support the flame, even at very high flow velocities. Additionally, the shear layers separating from the bluff body provide regions of slower-moving fluid for flame stabilization. Despite the benefits of these regions of strong shear and recirculation for static flame stabilization, these features can also result in instabilities in a bluff body flow field [2]. The unstable flow field can be further disturbed by the presence of acoustic forcing, resulting in high levels of flow oscillation that can lead to heat release rate oscillations in the flame through a velocity-coupling mechanism [3]. Feedback between flame heat release rate oscillations and acoustics in combustion systems can lead to thermoacoustic combustion oscillations, which can have harmful effects on the performance of gas turbine combustors and afterburners [4]. The goal of this work is to understand the impact of turbulent fluctuations on this velocity-coupled response in a rod-stabilized flame subject to acoustic forcing.

To understand the interaction of bluff-body stabilized flames and acoustic forcing, it is first important to consider the hydrodynamic instability behavior of the flow and the response of the flow to acoustics. Bluff body flows can display two hydrodynamic instabilities: the Kelvin-Helmholtz (KH) instability in the shear layers and the Bérnard von Kármán (BVK) instability in the wake [5]. The KH instability is a convective instability, which amplifies incoming disturbances, including acoustic disturbances. However, the BVK instability is a global instability, which acts as a self-excited oscillator and results in a large-scale anti-symmetric vortex street downstream of the bluff-body recirculation zone. The response of wake flows to acoustic forcing is complex, as the amplification of external disturbances by convectively and globally unstable flows are fundamentally different. Provansal et al. [6] showed that the shear layers of a bluff-body flow did respond to external excitation. However, the global instability is a self-excited oscillation whose response to external excitation could take many forms. For example, forcing a wake near or at its most unstable frequency can cause lock-in and amplification of the input disturbance [7]. Forcing at a frequency away from the natural vortex shedding frequency, however, can result in an insignificantly small response at the forcing frequency.

The presence of a flame can change the stability of the wake flow as well as its response to acoustic forcing through the presence of a density gradient, which changes the hydrodynamic stability characteristics of the flow. Linear stability analysis from Yu and Monkewitz [8] in a wake with a step profile showed the sensitivity of the system to both back-flow ratio and density ratio. Increasing back-flow ratio destabilized the wake, while increasing the density ratio stabilized the wake. Experimental work by Emerson et al. [9] showed this same trend occurs in a reacting wake, where a flame stabilized in the shear layers causes a density gradient between the centerline of the wake and the ambient fluid. Decreasing the temperature ratio across the flame using flow vitiation resulted in a density ratio near unity and more anti-symmetric wake oscillation. Similar results in large-eddy simulation were observed by Erickson and Soteriou [10]. Results from both Emerson et al. [11] and Erickson and Soteriou [10] showed that the stabilizing effect of the density gradient was dependent on the co-location of the density gradient (or flame) and the shear layer. By moving the flame further into the reactants and away from the shear layer, even a wake flow with a density ratio much greater than unity could display anti-symmetric vortex shedding in the wake.

At operating conditions where the density ratio is significantly greater than unity and is co-located with the shear layer, the flame response to acoustics is almost entirely determined by the shear layer response to acoustic forcing, as the global wake instability is completely suppressed. Experiments by Shanbhogue et al. [12] showed strong bluff-body flame response at the forcing frequency for a range of longitudinal acoustic forcing amplitudes. However, instances where the density ratio is close to unity or the flame is non-co-located with the shear layer, allowing some activity in the anti-symmetric vortex shedding mode, can have a complex response to longitudinal acoustic forcing. Emerson and Lieuwen [13] considered the dynamics of longitudinally-forced, near-unity-density-ratio bluff-body stabilized flames over a range of forcing frequencies. They showed that the response of the flame to symmetric acoustic forcing at the preferred mode of the wake resulted in both anti-symmetric and symmetric oscillations of the flame.

Put together, the response of the flame in a velocity-coupled system can be the result of many different velocity fluctuations. Some of these oscillations are coherent, including the vortices excited by acoustic forcing or the self-excited vortical oscillations that arise from the hydrodynamic instability in the flow field. Other oscillations are incoherent, particularly the turbulent oscillations that lead to flame wrinkling. The net effect of each disturbance on the flame, integrated over the length of the flame, determines the global heat release rate oscillation. Analysis by Preetham et al. [14] using a level-set formulation showed that the flame response at a given location is the result of both local and non-local disturbances. In a bluff-body stabilized flame, the local disturbance would arise from local flame wrinkling caused by vortices that convect along the flame. In any burner-stabilized flame, the non-local disturbance results from the imposition of the boundary condition on the flame, which creates a “root wave” or “base wave” that travels along the flame at a convection speed

that may not be equal to the vortical convection speed. Work by Humphrey et al. [15] explored the propagation of non-local disturbances along the flame front in a rod-stabilized, turbulent premixed flame. In this experiment, the rod oscillated transverse to the direction of flow, creating wrinkles that convected along the flame. These wrinkles are an example of non-local disturbances, as no acoustic forcing or vortex shedding was present in this experiment. Results from this work show the important impact that turbulence can have on the propagation of coherent, non-local flame wrinkles.

In systems with vortex shedding, like the one considered in this study, the formation of the vortex at the location where the flame is stabilized creates a root wave that propagates downstream as a non-local disturbance. The vortex also propagates downstream, creating local flame wrinkles, although the vortex propagation speed does not need to be the same as that of the root wave. As a result, interference patterns between the local and non-local disturbances can be observed in the flame area fluctuations and resultant heat release rate response along the length of the flame. These multiple disturbances are also the reason for nodes in the flame transfer function, which can occur when the local and non-local disturbances cancel each other out over the entire length of the flame, resulting in no global heat release rate response. Experimental observations of these cancellation phenomena are common in the flame-response literature [16–18].

Recent work by Æsøy et al. [19] has shown the impact that multiple vortical disturbances can have on axisymmetric bluff-body stabilized flames. In this experiment, a series of cylinders were placed in the annular passage upstream of the dump plane of the combustor to create vortical disturbances in presence of acoustic forcing. The flame, stabilized on a cylindrical centerbody, then saw the influence of the vortical disturbances from both the upstream cylinders and the vortex shedding at the edge of the centerbody, as well as the root wave. The phase between the two vortical disturbances was controlled by moving the set of cylinders relative to the dump plane to alter the convective time delay between vortex creation and impingement on the flame. The flame transfer function (FTF), a ratio of global heat release rate oscillations to input acoustic velocity oscillations, was measured at a range of frequencies. Both the amplitude of the FTF and the location of its peaks and troughs were varied by changing both cylinder location relative to the dump plane and flow velocity. Analysis of the FTF in the complex plane using phasors showed the key role that the phase between the two disturbances played in determining the global flame response. This configuration resulted in three disturbances on the flame – two local from the two vortical disturbances and one non-local from the root wave. The current study also has a three-wave configuration, although the source of the two local vortically-induced waves is different than in the work by Æsøy et al..

Further analytical work by Hemchandra and coworkers [20, 21] showed the mitigating role of turbulent fluctuations on the response of flames to longitudinal acoustic excitation. Hemchandra and Lieuwen [20] showed the impact of turbulence on local flame wrinkling in a rod-stabilized flame very similar to the configuration in the present study. Even in the absence of acoustic forcing, the non-local effect of the turbulent oscillations upstream of a given point, termed "memory effects" in the paper, modulate the oscillation of a turbulent flame at a given location. However, higher turbulent intensities result in shorter correlation length scales, such that the impact of the non-local disturbance decays more quickly due to the action of enhance kinematic restoration of the flame front. Experimental work by Chaparro et al. [22] and Kheirkhah and Gülder [23] both show the dramatic change in topology of bluff-body stabilized flames in the presence of turbulence. In Hemchandra et al. [21], this concept was extended to turbulent rod-stabilized flames with acoustic forcing, where turbulence was shown to both linearly and nonlinearly interact with the coherent wrinkles formed by acoustic forcing on a flame front. Here, the turbulence suppresses the coherent response of the flame to acoustic excitation through enhanced flame speed and faster kinematic restoration of flame wrinkles formed by coherent forcing. Very similar results are measured in the current experiments.

The current work considers the dynamics of a rod-stabilized flame at two different turbulence intensities. The flame is acoustically forced at the natural frequency of wake vortex shedding measured in the non-reacting case, as well as the first harmonic of that frequency. Flame heat release rate response is measured using high-speed CH* chemiluminescence. High-speed particle image velocimetry is used to measure the velocity field oscillations. We find that the flame response at the natural vortex shedding frequency is a superposition of multiple disturbances, including both symmetric and anti-symmetric vortex shedding present in the wake, leading to local constructive and destructive interference of flame heat release rate oscillations along the length of the flame. A simple analytical model is used to explain the source of this interference pattern. At the first harmonic, only the symmetric vortical disturbance is present, which significantly alters the local heat release rate dynamics. Implications for understanding thermoacoustic instability are discussed in conjunction with the results.

EXPERIMENT

Experimental Facility

The experiment consists of a rod-stabilized flame in a turbulent flow. The facility is pictured in Figure 1; the flow metering and control is described in more detail by Tyagi et al. [24] and this experimental configuration is described in more detail in Karmarkar et al. [25], so only a brief overview is provided here. In this experiment, fully-premixed air and natural gas ($> 95\%$ methane) at room temperature (300 K) and atmospheric pressure (1 atm) flow into a rectangular burner with cross-sectional

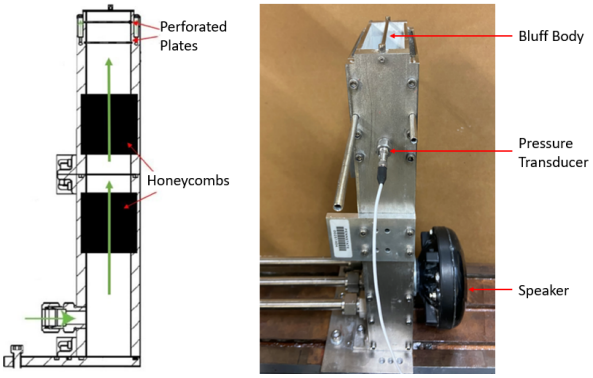

FIGURE 1. Experiment configuration.

dimensions of 30 mm $\times$ 100 mm. The fuel/air mixture flows through two ceramic honeycomb flow straighteners and the flame is stabilized on a 100 mm long, 3.18 mm diameter (D) rod that runs along the center of the burner. Turbulence is generated by perforated plates with a staggered hole pattern; the hole diameter is 3.2 mm and the open area of the plate is 40%. We test at two turbulence conditions, one without perforated plates and one with two perforated plates located 10 mm and 30 mm upstream of the burner exit. The in-flow fuel and air mixture is stoichiometric at all operating conditions in this study. However, local entrainment of ambient air into the mixture is expected, which means that the local equivalence ratio of the flame is likely lean. We do not attempt to account for any local variation in the equivalence ratio in this analysis, as the flame dynamics are not strongly dependent on equivalence ratio and we do not observe any local or global extinction as a result of this entrainment.

All data is obtained with a flow velocity of 10 m/s ($Re_D = 2036$). The configuration without perforated plates has an in-flow turbulence intensity of 5% and the configuration with two perforated plates has an in-flow turbulence intensity of 11%. More detailed characterization of the inflow turbulence is provided in Karmarkar et al. [25]. A speaker located upstream of the two honeycombs provides acoustic excitation of the flow and flame. The combination of a waveform generator and amplifier are used to generate the signal that drives the speaker. The acoustic excitation amplitude is modulated by varying the voltage on the waveform generator at a constant amplifier setting. The acoustic pressure fluctuation is measured using a piezoelectric pressure transducer (PCB 113B28) located upstream of the perforated plates. Pressure data is collected at 100 kHz for 1 second.

Diagnostics

High-speed stereo particle image velocimetry (PIV) is used to measure three components of velocity along the centerline plane of the experiment. A dual cavity, Nd:YAG laser (Quantronix Hawk Duo) operating at 532 nm illuminates aluminum oxide particles (0.5-2 microns) with a 50 mm wide, 1 mm thick sheet. Images of the particles are captured with two high-speed CMOS cameras (Photron FASTCAM SA5) in forward-forward scatter mode with the cameras at an angle of approximately 35 degrees relative to the laser sheet. Each camera is equipped with a 100 mm f/2.8 lens (Tokina Macro) and a Nikon tele-converter to allow for a safe stand-off distance between the sensor and the burner. Near-infrared filters (Schneider Kreuznach IR MTD) and laser line filters (Edmund Optics TECHSPEC 532 nm CWL) are used on each camera to reduce flame luminosity in the images. The field of view for the PIV data is 32 mm $\times$ 53 mm and data is collected at 10 kHz at each condition. Repeatability was tested across multiple days to ensure consistency in operating condition and diagnostics.

LaVision's DaVis 8.3 is used to perform vector calculations, which include a multi-pass algorithm with varying interrogation window sizes ranging from 64 $\times$ 64 to 16 $\times$ 16 and a 50% overlap. This processing results in a vector spacing of 0.48 mm/vector. The vector fields are post-processed using a universal outlier detection scheme with a 3$\times$3 median filter. The instantaneous uncertainties in the vector fields range from 1.5-2.8 m/s using the uncertainty calculation feature in Davis. The uncertainties in the RMS velocity range from 0.03-0.05 m/s in all cases. A total of 5000 vector fields are obtained for each condition.

The Mie-scattering images from PIV are also used to identify the flame location for calculation of a time-averaged progress variable, $\bar{c}$. The progress variable is defined as 0 in the reactants and 1 in the products, where the reactant and product regions are identified by the high and low seeding density, respectively. The process for binarization and edge detection in the Mie-scattering images includes five steps. First, images are Gaussian filtered for blurring sharp gradients due to noise. Second, median filtering with a window size of 10 pixels $\times$ 10 pixels is applied to remove the effect of salt and pepper noise due to scattering from aluminum oxide particles. Next, a smoothing operation is performed using bilateral filtering, and then Otsu's method is applied on the smoothed image and multi-level thresholding is used to account for the spatial variation in signal intensity; the number of thresholds is varied between four and eight depending on the conditions. Finally, the minimum threshold value is used to binarize the processed image into a value of 0 in the reactants and 1 in the products.

High-speed chemiluminescence imaging is used to measure the heat release rate fluctuations of the flame. We use a high-speed camera (Photron FASTCAM SA4) coupled with a UV intensifier (Invisible Vision UVi) to capture images at 4 kHz for one second. Chemiluminescence data has a field of view of 241 mm $\times$ 148 mm. A filter with a center wavelength of 430 nm and filter width of $\pm$10 nm is used to isolate the signal from CH* chemiluminescence. As mentioned previously, the local equivalence ratio of the flame likely varies along the length of

the flame due to entrainment of ambient gases. Previous studies of partially-premixed flames like this one have shown that CH* chemiluminescence is a good marker of local heat release rate fluctuations [26, 27].

Data Analysis

Acoustic forcing amplitude at the forcing frequency is determined using a fast Fourier transform (FFT) of the signal from the pressure transducer upstream of the flame. We extract the coherent component of the pressure signal by performing a triple decomposition on the time varying signal. In statistically-stationary flows, any flow variable, $f(x,y,t)$, can be decomposed into three components: a time-averaged value, a coherent component, and an incoherent, or turbulent, component [28], as shown in Eq. 1.

$$f(x,y,t) = \bar{f}(x,y) + \tilde{f}(x,y,t) + f'(x,y,t) \quad (1)$$

In this work, we extract the coherent component by computing the fast Fourier transform of the time-varying signal and extracting the signal content corresponding to the acoustic forcing frequency. We do this because the acoustic forcing is the primary source of coherent oscillations in the signal. We also apply the triple decomposition method to the intensity signal obtained from the CH* images. This method allows us to study the development of coherent heat release oscillations in the downstream direction.

The phase-averaged progress variable contours are computed by averaging binarized images at each phase, where each phase has 290 images. Since the frequency of acoustic forcing, $f_0 = 580\ Hz$, is not an integer multiple of the sampling frequency ($f_s = 10\ kHz$), we interpolate between images to obtain multiple images at a single phase. To do this interpolation, we use a non-rigid image registration algorithm to compute the flame location at the appropriate time between one image and the next. The non-rigid image registration method uses the `imregdemons` function in MATLAB and calculates a displacement field from one image to the next that can then be scaled to determine the intermediary flame location. This method was previously used in our group by Tyagi et al. [29]; this reference contains a more detailed discussion of the method and the supplementary material includes a thorough sensitivity and uncertainty analysis associated with non-rigid image registration.

RESULTS

Test Conditions

The test matrix is designed to understand the impact of turbulence intensity on the heat release rate response of a flame to acoustic forcing at a variety of intensities. In all cases, the time-averaged flow velocity is 10 m/s and two turbulence intensities are considered: 5% and 11%. The 5% turbulence intensity condition is generated without the use of perforated plates, whereas the 11% turbulence intensity condition is generated with two perforated plates. The equivalence ratio is unity throughout and the mixture of natural gas fuel and air is perfectly premixed far upstream of the experiment. Further details about the flow operating conditions are described in Karmarkar et al. [25].

We study the heat release rate response at varying amplitudes of acoustic excitation at two frequencies – the natural frequency of vortex shedding for the cylindrical bluff body, 580 Hz, and the frequency of its first harmonic, 1160 Hz. The natural frequency of vortex shedding is identified to be 580 Hz from analysis of the non-reacting flow at the same conditions. Further discussion of the non-reacting flow dynamics and the impact of the flame on the flow instabilities can be found in Karmarkar and O'Connor [30]. Prior work by Emerson and Lieuwen [13] showed that response of a bluff-body stabilized flame to forcing at the first harmonic of the most unstable frequency resulted in more complex dynamics, which will be discussed in the context of our results.

Figure 2 shows the coherent pressure fluctuation amplitude measured upstream of the bluff body and the perforated plates as a function of waveform generator voltage for both the low-turbulence (0 plates) and high-turbulence (2 plates) conditions at the 580 Hz forcing condition. The amplitude of acoustic forcing increases linearly with the voltage of the waveform generator. Further, there is not a significant difference between the acoustic amplitude with and without plates present, indicating that the upstream boundary condition is the same for both conditions. Acoustic velocity fluctuations for these conditions at the exit of the experiment are also the same for both plates, as was discussed in [31]. Figure 3 shows the same result for forcing at the first harmonic, 1160 Hz. Note that for the higher frequency, the presence of the perforated plates attenuates the acoustic forcing at this higher frequency, which is not unexpected. For voltages between 0 and 6 Volts, the acoustic amplitude for the two plate conditions is very similar. At higher voltages, the presence of the perforated plates attenuates the acoustic forcing. However, there are two conditions where the acoustic amplitude is similar and so will be directly compared in this analysis: 10 V/0 plates and 14 V/2 plates ($\approx$ 0.1 kPa), and 14 V/0 plates and 20 V/2 plates (0.13 kPa).

Time-Averaged Flame Structure

The time-averaged flame shape, as measured using CH* chemiluminescence imaging, is shown in Figure 4. In this figure, the low turbulence intensity cases are shown on the top row and the high turbulence intensity cases are shown on bottom row. The left column represents conditions with no acoustic forcing and the right column depicts conditions with maximum amplitude acoustic forcing. As the turbulence intensity is increased, the flame stabilizes at a wider angle. This change in flame angle is a result of higher turbulent flame speed due to more intense

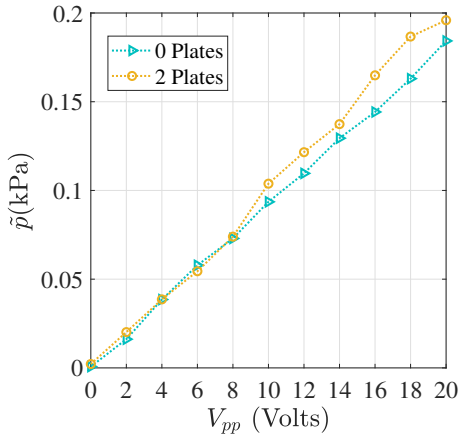

FIGURE 2. Amplitude of acoustic pressure fluctuations at forcing frequency as a function of input voltage (V_{PP}) for $f_0 = 580Hz$.

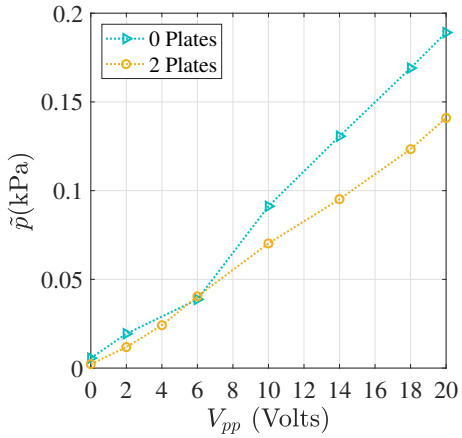

FIGURE 3. Amplitude of acoustic pressure fluctuations at forcing frequency as a function of input voltage (V_{PP}) for $f_0 = 1160Hz$.

turbulent flame wrinkling. As the acoustic forcing amplitude is increased, the flame angle is enhanced slightly as well. The high-intensity acoustic forcing modulates the flame position over the course of an acoustic cycle, leading to a wider flame brush as well as a slightly higher turbulent flame speed. These changes in flame brush and flame speed with acoustic forcing are well documented in literature [21].

Figure 5 shows the time-averaged CH* signal intensity for the cases with forcing at the first harmonic. Like before, the low turbulence intensity conditions are shown in the top row and the high turbulence intensity conditions are shown on the bottom row. The left column shows the case with no acoustic excitation and the right column depicts conditions with maximum amplitude of acoustic excitation. Like in the fundamental forcing cases, the flame stabilizes at a wider angle in the high-turbulence conditions when compared to the low-turbulence conditions. The acoustic forcing does not significantly impact the time-averaged CH* images, other than a slight thickening of the flame brush. The time-averaged images resemble the fundamental forcing conditions, which is to be expected since the forcing frequency will primarily only change the dynamic behavior of the flame.

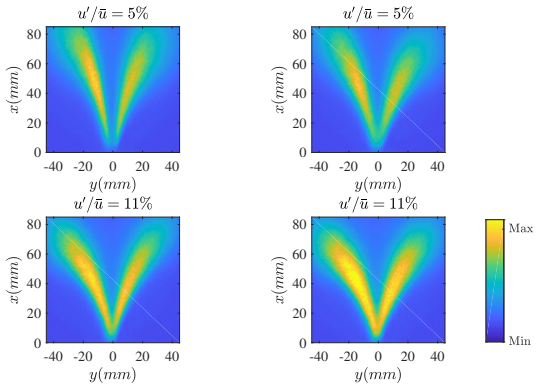

FIGURE 4. Time-averaged CH* image, for the low (top) and high (bottom) turbulence intensity conditions with no acoustic forcing (left) and maximum acoustic forcing (right) for $f_0 = 580Hz$

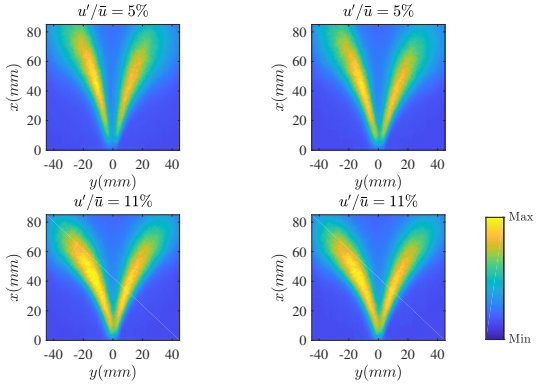

FIGURE 5. Time-averaged CH* signal intensity for the low (top) and high (bottom) turbulence conditions with no acoustic forcing (left) and maximum (right) acoustic forcing for $f_0 = 1160Hz$.

Flame Response to Fundamental Forcing Frequency

The time-averaged images of the flame chemiluminescence indicate that turbulence impacts the flame structure and flame brush thickness. However, to understand how the coherent oscillations in the heat release rate are modulated by the presence of acoustic and hydrodynamic perturbations, we observe the frequency-domain response of the flame. We use the flame edge locations extracted from the Mie scattering images to identify the instantaneous location and structure of the flame. The flame edge locations at each instance are obtained from binarization of the

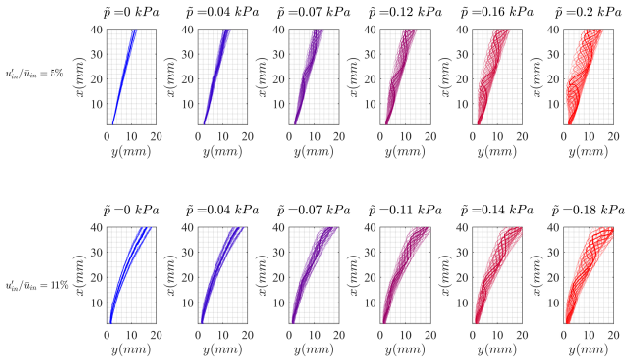

FIGURE 6. Phase-averaged progress variable contours ($\tilde{c} = 0.5$) at varying levels of acoustic excitation for low turbulence intensity conditions (top row) and high turbulence intensity conditions (bottom row) for $f_0 = 580Hz$.

Mie scattering images from the PIV measurements. To capture the coherent response of the flame edge fluctuation, we compute the phase-averaged progress variable contour at the forcing frequency $f_0 = 580\ Hz$. Figure 6 shows the phase-averaged flame edge ($\tilde{c} = 0.5$) at varying phases for half the flame. The dotted lines represent the extent of the phase-averaged flame brush, $\tilde{c} = 0.7$ and $\tilde{c} = 0.3$, for all phases. The phases are superimposed to provide a visual representation of the development of the wrinkle amplitude with downstream distance. In the absence of acoustic excitation, the edges at all phases collapse to the time-averaged flame location, indicating that there are no coherent wrinkles on the flame edge, which is to be expected.

In the absence of acoustic forcing, the phase-averaged flame brush is thicker in the high-turbulence condition than in the low-turbulence conditions. This difference is due to the fact that increasing turbulence causes increased flapping and small-scale wrinkling of the flame front. At the highest acoustic forcing for the low-turbulence condition, the coherent wrinkles form sharp cusps in the upstream region, which are then smoothed out as they convect downstream. By comparison, in the high-turbulence condition, the coherent wrinkles are more rounded and have a smaller amplitude of oscillation in the near-wake region. There are two reasons for this trend. First, with increasing turbulence, the increased flame speed causes the flame to stabilize at a wider angle (see Fig. 4), which increases the spatial separation between the flame and the shear layer, where vortical disturbances are generated. Second, the vortical disturbances themselves are weaker in the high-turbulence conditions when compared to the low-turbulence conditions. This result has been shown previously in the literature [32] and has been seen to be true for this configuration as well [30].

It is interesting to note, however, that in the low-turbulence conditions, at all excitation amplitudes, the coherent wrinkle amplitude is comparable to the width of the phase-averaged flame brush amplitude, indicating that the cycle-to-cycle variation in the flame edge location is low in these conditions. By contrast, the high-turbulence conditions show a phase-averaged flame brush that is visibly wider than the wrinkle amplitude. This effect is known as phase jitter, and it can be seen that increasing turbulence increases the magnitude of jitter [33]. Turbulence can have two effects on coherent structures: it can cause more rapid decay of the peak vorticity through turbulent diffusion, as noted above, and it can move the structures in space, which is a process referred to as phase jitter. Since the $\tilde{c} = 0.5$ contours are phase-averaged using a Fourier transform, we capture the coherent effects from the jitter of the flame front, which is a function of both flame response to the turbulence and increased jitter in the coherent structures convecting along the flame surface.

To quantitatively characterize the amplitude of coherent oscillations of the flame edge, we use the envelope of the flame edge oscillations, shown in Fig. 6, and compute a wrinkle amplitude, w_f, at every location along the $\bar{c} = 0.5$ contour. We do this by computing the normal distance from the $\bar{c} = 0.5$ contour to the edges of the envelope of the flame wrinkles at every location along the flame length (l_f). The plots in Fig. 7 show the development of the wrinkle amplitude, w_f, along the flame length at all excitation amplitudes for both turbulence intensities. In the absence of acoustic excitation, the coherent wrinkle amplitude for both turbulence intensities is negligibly small, but as the acoustic excitation amplitude increases, the wrinkle development in the low- and high-turbulence conditions is different. Close to the bluff body ($l_f < 5mm$), the wrinkle amplitude development is independent of turbulence intensity. In this region, the flame dynamics are governed primarily by the flame holding boundary condition enforced by the bluff body. Further downstream, with increasing acoustic excitation, the wrinkle amplitude increases for both turbulence intensities, but the coherent wrinkle growth is faster in the low-turbulence condition. This faster growth is due to the fact that the coherent flow oscillations are stronger in this condition and the flame is closer to the shear layer. At high excitation amplitudes, the coherent wrinkle amplitude in the low-turbulence condition saturates in the far-field region ($l_f > 20$ mm). The coherent response saturation is due to the decay of coherent vortices downstream and the smoothing of wrinkles due to kinematic restoration. Details of this process were shown in both experiments and nonlinear level-set modeling by Shanbhogue et al. [12]. Interestingly, the saturation limit of the flame at the high-turbulence condition has not been achieved in the field of view. The lack of saturation is likely a consequence of increased phase jitter, which allows the coherent wrinkle amplitude to grow downstream, since the cycle-to-cycle location of the edges is varying.

The analysis of the coherent flame wrinkling shows that the presence of turbulence can significantly impact the heat release

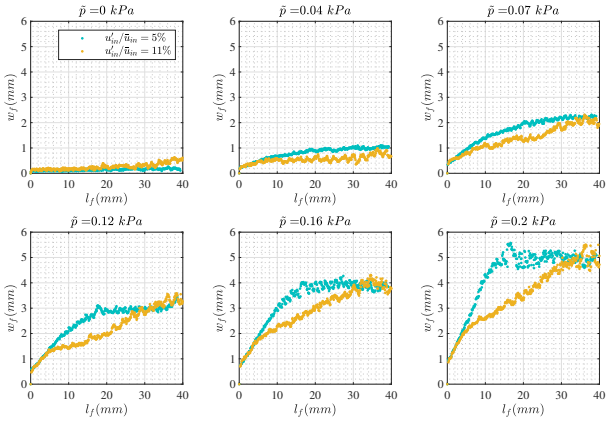

FIGURE 7. Coherent wrinkle amplitude development along the flame length (l_f) for varying levels of acoustic excitation for the low (blue) and high (yellow) turbulence intensities for $f_0 = 580Hz$.

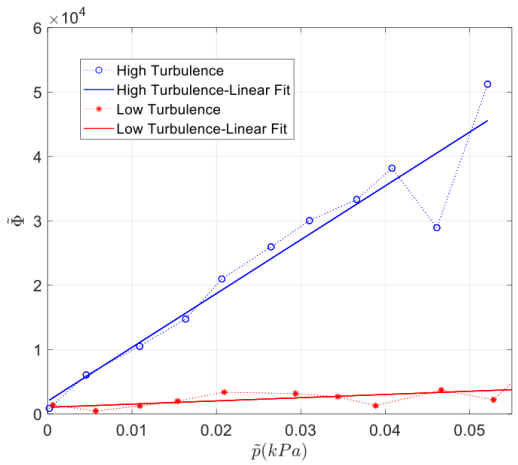

FIGURE 8. Coherent component of the spatially integrated CH* signal intensity fluctuation for both low- and high-turbulence conditions with varying amplitudes of acoustic pressure for $f_0 = 580Hz$.

response of the flame by modulating the local and non-local coherent oscillations in the flame surface area. This analysis quantitatively illustrates that the coherent wrinkling of the flame is sensitive to the presence of turbulence. A detailed analysis of the flame brush is provided in Karmarkar and O'Connor [31]. While this analysis is extremely useful in understanding the mechanisms by which coherent wrinkling occurs, this analysis is not sufficient to capture the entire flame response for several reasons. First, the edges from the Mie-scattering only measure lateral flame displacement, which ignores the multi-valued behavior that is seen at high amplitudes. Second, the actual flame area is enhanced by the turbulence, which wrinkles the flame on finer scales than can be measured with the Mie-scattering edges. Finally, flame stretch locally changes heat release rate oscillations, which would not be captured in the Mie-scattering edges. We expect that the heat release rate response is greater in the chemiluminescence measurement than the lateral flame displacement measurement because the chemiluminescence captures all these turbulent flame behaviors.

We use the fluctuation of the CH* signal intensity to quantify the oscillations in the rate of heat release from the flame. Figure 8 shows the variation in the global coherent CH* fluctuation with coherent pressure fluctuation for the low- and high-turbulence conditions with varying levels of acoustic excitation amplitude, $\tilde{p}$. The global coherent CH* fluctuation is calculated by first summing the CH* signal over the region of interest in the image and then applying the triple decomposition to calculate the coherent oscillation. In Fig. 8, the heat release rate response varies almost linearly with input acoustic excitation. However, for the same excitation input, the overall coherent response in the high-turbulence condition is higher than that of the low-turbulence condition. From the analysis of the scattering images in previous section, we know that high turbulence conditions have a more cycle-to-cycle variation, causing a thicker coherent flame brush. This means that the coherent content is more spread out in space and this can potentially lead to higher values in a spatially integrated measure like CH* chemiluminescence. Further, the higher turbulence intensity enhances the flame area through wrinkling, increasing the overall signal level as well as the fluctuation levels.

Figure 9 shows the evolution of coherent CH* fluctuations with downstream location for both turbulence conditions at a range of forcing amplitudes. To obtain this plot, we use the right half of the V-flame and divide the image into 52 sections in the streamwise direction. We then average the signal in every 'section' and then perform a triple decomposition on this spatially-averaged, time-varying signal. In this way, we extract the coherent component at every downstream location. Results from the right-half of the flame and the left-half of the flame produce the same results. Figure 9 shows the amplitude of coherent fluctuations normalized by the total RMS fluctuation of all three velocity components. We do this normalization because the high-turbulence cases will have more overall fluctuations, so in order to truly compare the coherent parts across the low- and high-turbulence conditions, a normalized metric is more useful.

The heat release rate response in Fig. 9 follows an oscillating decay pattern and periodic nodes can be seen in the response curves. This response is indicative of interference in the coherent oscillations that drive the heat release rate fluctuations. In this acoustically-forced, rod-stabilized flame, there are three potential sources of coherent oscillations at the frequency of excitation. First, the acoustic excitation drives a symmetric vortex shedding mode that locally modulates the flame surface area, driving oscillations in the heat release rate. The second driver of

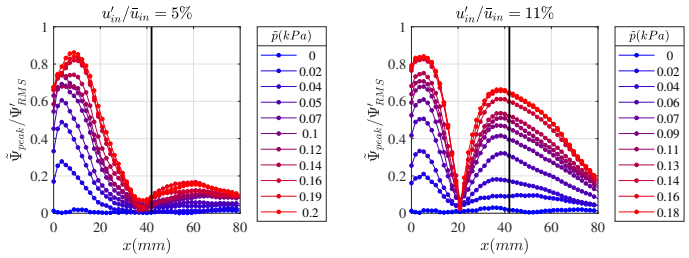

FIGURE 9. Coherent component of CH* intensity fluctuation ($\tilde{\Psi}$) normalized by the RMS of the total intensity fluctuation (Ψ_{RMS}) for different levels of acoustic excitation for the low- (left) and high- (right) turbulence conditions for $f_0 = 580Hz$. The black line denotes the limits of the PIV measurements.

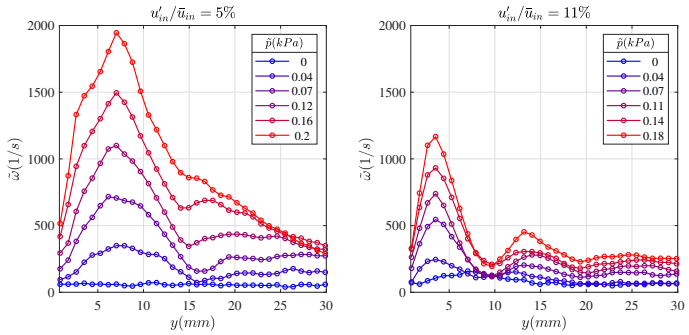

FIGURE 10. Coherent vorticity response along the shear layer for both low- (left) and high- (right) turbulence conditions for varying amplitudes of excitation for $f_0 = 580Hz$.

coherent oscillation is the non-local "memory" effect, where a coherent wrinkle in the flame surface area generated at the base of the flame convects downstream along the flame contour; this wrinkle is often referred to as the "base wave" or "root wave," and is generated by the acoustically-driven vortex at the flame attachment point. This non-locality occurs due to the presence of a mean tangential velocity along the flame brush, which can cause wrinkles generated at one location to move downstream along the flame. Finally, a third source of coherent fluctuations in this particular configuration is the local modulation of the flame surface area caused by the natural anti-symmetric BVK vortex shedding mode, which is present at this frequency since the frequency of excitation is set to match the natural frequency of vortex shedding. Even though the two vortex shedding modes are occurring at the same frequency, they are out of phase and convect at different speeds, which can cause local interference effects and impact the local vorticity field in the flow, which will then impact the local flame area fluctuations.

To illustrate this point, Fig. 10 shows the downstream evolution of vorticity along the shear layer, from Karmarkar and O'Connor [30]. The coherent vorticity is computed using the PIV data at every downstream location along the shear layer. The vortical response, like the CH* response, also exhibits an oscillating decay pattern. In the vorticity field, the interference pattern is formed as a consequence of the interaction between the symmetric and the anti-symmetric vortex shedding modes at this condition. Increasing the coherent excitation amplitude leads to a monotonic increase in the response amplitude, but does not significantly impact the basic shape of the curve. However, increasing the free stream turbulence significantly changes the decay pattern as well as the location of the nodes. A detailed analysis of the vorticity response is provided in Karmarkar and O'Connor [30]. The interactions between the three coherent flame oscillations – the non-local root wave, the local symmetric vorticity disturbance, and the local anti-symmetric vorticity disturbance – ultimately create the interference pattern seen in Fig. 9.

The flame response is directly impacted by varying the turbulence levels in two ways. First, increasing turbulence intensity increases the turbulent flame speed, which causes the coherent flame wrinkles to be smoothed out over a shorter timescale and causes the flame to be stabilized away from the shear layer. Second, increasing turbulence can cause flapping of the flame front, which leads to a cycle-to-cycle variation in the coherent flame edge, as discussed previously. In addition to the direct impacts, turbulence can also impact the heat release rate indirectly by modulating the local vorticity field in two ways. First, increasing levels of turbulence can weaken the strength of the coherent vortices being shed from the bluff body. This result has been shown in the literature [32] and is verified to be true in this configuration as well, as shown in Fig. 10. Second, our vorticity analysis shows that, while increasing the free stream turbulence weakens symmetric vortex shedding mode, it can actually enhance the natural anti-symmetric vortex shedding mode [25]. Combined, these effects have a complex, nonlinear impact on the coherent heat release response.

In order to describe the individual and combined effects of the three drivers of coherent disturbances – local symmetric fluctuations in vorticity, non-local memory effects of symmetric fluctuations from the root disturbance, and local anti-symmetric vorticity fluctuations from the natural vortex shedding mode – we use a simple conceptual model to understand how these disturbances interact and to study their individual effects on the coherent heat release response.

Reduced-Order Model

The conceptual model provided here is for illustrative purposes to establish the governing parameters that determine the shape of the response curve. To understand the interaction between the three disturbance sources, we construct a waveform by superimposing three sinusoidal waves oscillating in space and time. A stationary linear growth and exponential decay envelope is applied to each waveform in the spatial domain. The growth

of coherent disturbance is caused by the formation and development of vortices shed from the bluff body [34]. The strength of the vortex increases linearly in the spatial domain until the vortex development length. The decay of the coherent disturbance field is primarily governed by thickening of the shear layer and gas expansion effects. For the purposes of this analysis, we assume that the wave amplitudes are constant in time. The waves are described as follows:

$$s_1(x,t) = Axe^{-Bx}e^{i(kx-\omega t)} \tag{2}$$

$$s_2(x,t) = xe^{-Bx}e^{i(Ckx-\omega t-\Delta\phi)} \tag{3}$$

$$s_3(x,t) = nAe^{-B\alpha x}e^{i(Kkx-\omega t)} \tag{4}$$

$$S(x,t) = s_1(x,t) + s_2(x,t) + s_3(x,t) \tag{5}$$

Here, x and t are the variables representing space and time, respectively. The first waveform, s_1, is representative of the acoustically-induced symmetric vortex shedding, which acts as a local disturbance to the flame. The parameter B controls the decay rate of this disturbance in the spatial domain. Waveform s_2 represents the naturally occurring hydrodynamic instability mode, which manifests as an anti-symmetric vortex shedding mode. The waveform s_2 has a phase difference $\Delta\phi = \pi$ with respect to s_1 since the symmetric and anti-symmetric waves are out-of-phase with each other at the vortex shedding location at the trailing edge of the bluff body. Parameter A governs the relative amplitude of the acoustically excited mode as compared to the natural vortex shedding mode. As acoustic excitation increases, the value of parameter A increases as well. Both waves s_1 and s_2 have the same frequency of oscillation in time, $\omega = 2\pi f_0$, where f_0 is the frequency of oscillation. The spatial wave number k is defined as $k = 2\pi f_0/\bar{u}$, where $\bar{u}$ is the mean flow speed. Parameter C is the ratio of the spatial wavelengths of s_1 and s_2. The parameters of the analytical model are matched with those from the data as closely as possible. In this model, B is set to 300 to match the decay envelope of the time-averaged vorticity field. For simplicity, we set B to be the same for all waves even though in reality it will be different. In this model, $0 < x < 0.05$, $f_0 = 580\ Hz$, and $k = 2\pi f_0/\bar{u}$, where $\bar{u} = 10\ m/s$. The parameter C is set to 2.5 to match the vorticity response.

Finally, waveform s_3 represents the non-local memory effect. Here, parameter n governs the relative amplitude of the non-local effects when compared to the local effects. Parameter K is a convection parameter defined in Preetham et al. [14].

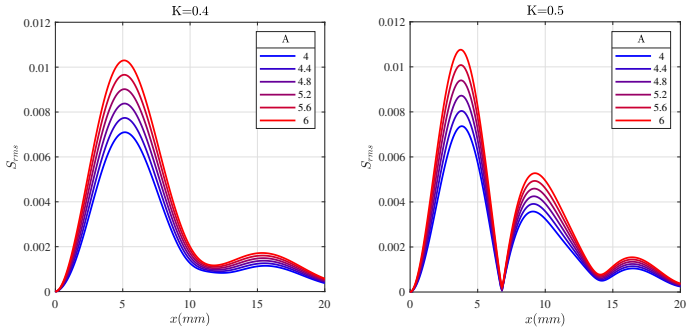

FIGURE 11. Plots of the response fluctuation S_{rms} from the three-wave interference model for varying values of parameters K and A for forcing at the fundamental frequency.

Parameter K determines the ratio of the mean flow velocity to the disturbance propagation speed u_c along the flame, $K = \bar{u}/u_c$. In reality, both the symmetric and anti-symmetric disturbances should contribute to the non-local component, but the symmetric mode is significantly stronger than the anti-symmetric mode. So for the purposes of this analysis, we assume that the non-local disturbances created as a consequence of the symmetric wave travelling along the flame front. For the non-local effects, we add an additional factor α to the decay envelope. We do this so that we can vary the rate at which the convected disturbances are being dissipated due to kinematic restoration and small scale turbulent motion in the flame. Superimposing the three waves, the total response S is computed for varying levels of the parameters K, A, α, and n. We find that parameter A governs the response amplitude, but does not impact the node spacing or the shape of the curve. Varying parameter α changes the response amplitude and the decay of the response with downstream location. Varying n also changes the amplitude and decay pattern. Most importantly, parameter K changes spacing of the node pattern. The model is most sensitive to the value of parameter K. Results of previous level-set simulations have shown a similar strong sensitivity of flame response to K [14].

The response curves shown in Fig.9 show that changing the turbulence level changes the spatial wavelength or node-spacing of the interference pattern in the response. This change suggests that parameter K is varying between the low- and the high-turbulence conditions. Figure 11 shows the model response for two values of parameter K and varying levels of parameter A for each K. These plots are very similar in shape to the experimental results shown in Fig. 9. Varying amplitude A is effectively the same as increasing coherent excitation input. In the plots shown in Fig. 9, the parameter n is set to 1 and $\alpha = 1$. In general, parameters n and α do not change the response significantly. These parameters are set so that the model plots match the plots from the results, which is helpful for understanding the results.

From the plots shown in Fig. 11, it is evident that changing

the turbulence level slightly increases the parameter K, which is the ratio of the mean flow velocity to the convective phase speed of the disturbance. Since the mean flow velocity is held constant in these tests, the model suggest that increasing turbulence is essentially causing a decrease in the convective speed of the disturbances as they move tangential to the flame front. To understand why this is the case, consider the time-averaged images shown in Fig. 9. The location at which the flame is stabilized is a function of the mean flow velocity $\bar{u}$ and the turbulent flame speed S_T, which governs the rate at which the flame propagates normal to itself. Increasing turbulence increases S_T, which does not directly impact the convective phase speed, since that is governed by the tangential velocity along the flame. However, the for a uniform mean flow, with no transverse components, the tangential convective velocity of disturbances along the flame front is given by $U_e \propto \cos(\theta)$ (see [35]), where θ is the wedge angle of the flame. As shown in Fig. 4, since increasing the turbulence level increases S_T, this in turn increases θ. If $\bar{u}$ is held constant, then the flame is stabilized at a wider angle for higher levels of S_T. This increase in θ leads to a decrease in the speed with which disturbances travel along the flame, since the tangential convective speed is directly proportional to $\cos(\theta)$ and for values $\theta < 90^o$, increasing θ decreases $\cos(\theta)$.

It is important to note that the nature of the response is extremely sensitive to K, which means that even small increases in wedge angle can fundamentally modulate the nature of the response. This highly simplified conceptual model helps interpret the results we see in the CH* data and identifies how the many varying parameters impact each other and ultimately the heat release rate response. This analysis shows that, in this three-disturbance model, varying turbulence levels has a significant impact on the how the vortically-induced wrinkle in the flame is convected along the flame. Combined with the experimental results, the model provides useful insight into how turbulence can impact the flame response when forced at a frequency equal to the natural frequency of vortex shedding.

Heat Release Response for $f_f = 2f_0$

The results from the fundamental frequency forcing conditions illustrate how the presence of turbulence can impact the nature of the coherent heat release. We now consider the conditions where the flame is forced at twice the natural frequency of vortex shedding. This case is interesting because, unlike the fundamental forcing case, in this case the coherent response is not impacted by the presence of a natural anti-symmetric vortex shedding mode. This analysis was motivated by previous results from Emerson and Lieuwen [13], who analyzed the dynamics of the flame at the first harmonic of the longitudinal acoustic forcing frequency.

Like in the fundamental forcing case, we compute a spatially-integrated, coherent fluctuation of the CH* images to characterize the response at each condition. Figure 12 shows the coherent component for varying levels of acoustic excitation and turbulence condition. The curves here look significantly different than the fundamental forcing case. In this case, the presence of turbulence actually decreases the coherent response. This suppression is potentially due to the fact that, in the absence of a hydrodynamic mode, the vortical disturbances generated by the acoustic forcing decay faster in the high-turbulence conditions as compared to the low-turbulence conditions due to the kinematic restoration effect. Here, the flame wrinkles generated by the higher-frequency vortical disturbances have a shorter wavelength, and so they are annihilated more quickly by the action of kinematic restoration. Since the vorticity in this case is predominantly due to the symmetric vortex shedding mode, the presence of turbulence suppresses the spatially integrated response. It should also be noted that the amplitude of the coherent response, in general, is lower than in the fundamental forcing case. This is to be expected since the flame acts as a low-pass filter in the frequency domain.

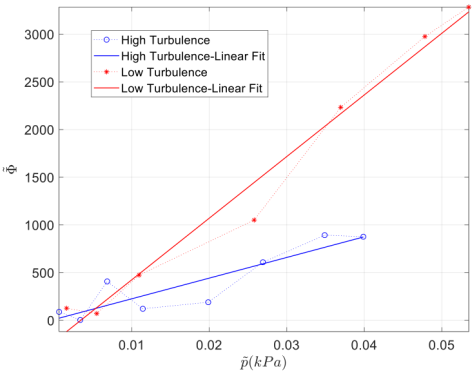

FIGURE 12. Coherent component of the spatially-integrated CH* chemiluminescence signal intensity for both turbulence conditions at all excitation amplitudes for first-harmonic forcing for $f_0 = 1160Hz$.

To understand how the response evolves with downstream distance, we again compute the coherent response by integrating over smaller sections in the downstream direction. Figure 13 shows the spatial decay of coherent oscillations in the heat release. Again, the nature of the curves exhibits an oscillating decay pattern and nodes can be seen in the response. However, there are significant differences when compared to the response at the fundamental forcing conditions. First, the spatial wavelength of the interference pattern does not significantly vary between the low- and the high-turbulence conditions. The nature of the decay is different, but the node spacing is fairly similar. This similarity indicates that, in this case, parameter K is not a governing parameter, which may be due to the fact that the disturbances decay too quickly in the high-frequency forcing conditions, so the memory effect is not the dominant driver for the coherent re-

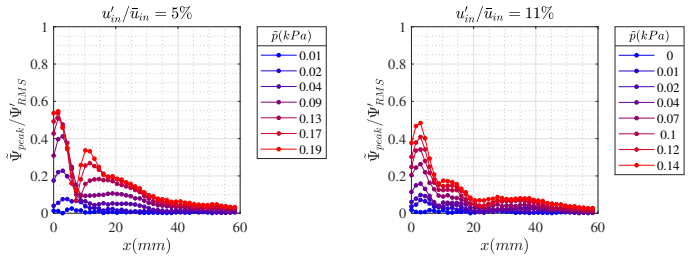

FIGURE 13. Coherent component of the CH* intensity fluctuation normalized by the RMS of the total intensity fluctuations for varying levels of acoustic excitation for the low- (left) and high- (right) turbulence conditions at first-harmonic forcing conditions for $f_0 = 1160Hz$.

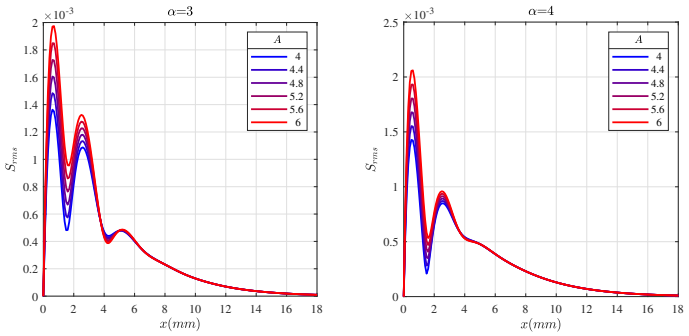

FIGURE 14. Plots of the response fluctuation amplitude from conceptual model for forcing at $f_0 = 1160Hz$.

sponse. Second, compared to the fundamental forcing cases, the relative response amplitudes are also lower overall. For the same excitation amplitude, the near-field response is fairly comparable between the low- and high-turbulence conditions. In this region, the flame response is dominated by the flame holding more than the vortical coupling. Further downstream, the second response peak in the low-turbulence case is stronger and more distinct than in the high-turbulence case. This result suggests that in the case of the first-harmonic forcing, the response is primarily governed by the decay rate of the oscillations.

It should also be noted that, unlike the fundamental forcing conditions, the coherent response curves in these conditions are more noisy and the trends are not as smooth, especially at low forcing amplitudes. This difference is partly due to the fact that the excitation input in these conditions is weaker and also due to the fact that the disturbance in this case has a shorter wavelength and a faster decay rate, which lowers the signal-to-noise ratio. Like in the case with fundamental forcing, we once again use a conceptual model to interpret the results from Fig. 13. We use the same model as before with the exception that, in this case, we do not use the anti-symmetric mode waveform, so this is a two-wave interference model and $s_2(x,t) = 0$. In this case, the parameter K, while important to establish the shape of the curve, is not the governing parameter that drives the differences between the low- and high-turbulence responses. We find that it is α, which is the decay rate of the spatial envelope for the non-local term relative to the local disturbance, that drives the differences in the low- and high-turbulence cases. Increasing turbulence causes the disturbances to decay more quickly due to small-scale wrinkling. When the disturbances decay on a shorter length scale, then the impact of the non-local effect is reduced as well.

Figure 14 shows plots of the response RMS as a function of the downstream coordinate for varying levels of amplitude A. In this case, amplitude A is simply an amplification factor and can be compared to the excitation input amplitude. The plot on the left is for a lower value of parameter α and is comparable to the low-turbulence response as shown in Fig. 13. As the value of α is increased slightly, the decay of the response changes and begins to resemble the high-turbulence condition. This simplified model suggests that at the first harmonic forcing condition, the main effect of turbulence is to enhance the decay of local disturbances as they convect along the flame front. While the agreement between the model and the experimental measurements is not as good as in the fundamental case because of the low signal-to-noise ratio in these conditions, the plots in Fig. 14 still provide useful information about the possible dominant governing parameters that drive the difference between the low- and high-turbulence responses.

CONCLUSIONS

The focus of this work is to characterize how turbulent fluctuations can impact the coherent heat release rate oscillations of a acoustically-excited flame. We study the response of a flame to acoustic forcing at two frequencies – the fundamental frequency of vortex shedding and its first harmonic – at two turbulence intensities. By studying the downstream development of the heat release rate response, we find that the mechanisms driving the coherent response are strongly dependent on the frequency of forcing. In the conditions where the forcing frequency is equal to the natural frequency of vortex shedding, the response is governed by three harmonic disturbances on the flame: the non-local root wave, the local symmetric disturbance from the symmetric vorticity mode, and the local anti-symmetric disturbance from the anti-symmetric vorticity mode. Using a simplified conceptual model, we show that the increase in free-stream turbulence changes the coherent response by impacting the speed with which the disturbances propagate along the flame. In the first-harmonic forcing conditions, however, the parameter dependencies are different. At these conditions, turbulence changes the response by impacting the length scales at which the disturbances decay with downstream distance.

This work is a step towards comprehensively characterizing the impact of turbulent fluctuations in different regimes of acous-

tic perturbation. In particular, this work shows the many pathways by which turbulence affects flame response. Turbulence modifies the behavior of coherent vorticity through noise-forced excitation of the anti-symmetric wake shedding model as well as turbulent diffusion of coherent vorticity in the flow. Turbulence also changes the flame speed and the flame area, which modify the shape of the flame and its relative position to the vortical oscillations. Further, modification of the flame shape changes the convection speed of wrinkles along the flame, which impacts the interference patterns between the local and non-local disturbances on the flame surface. Finally, turbulence enhances the flame area and heat release rate through small-scale wrinkling and stretch effects, which modify the amplitude of heat release rate oscillations for a given input acoustic disturbance. These multiple pathways by which turbulence modifies flame response should be considered in low-order modeling of thermoacoustic instability, particularly in combustors where turbulence intensities are high.

ACKNOWLEDGMENT

This work was supported by National Science Foundation grant CBET-1749679. Any opinions, findings, and conclusions or recommendations expressed in this material are those of the authors and do not necessarily reflect the views of the National Science Foundation.

REFERENCES

[1] Lefebvre, A. H., and Ballal, D. R., 2010. *Gas turbine combustion: Alternative fuels and emissions*. CRC Press.

[2] O'Connor, J., 2022. "Understanding the role of flow dynamics in thermoacoustic combustion instability". *Proceedings of the Combustion Institute,* ***in press***.

[3] Schadow, K., and Gutmark, E., 1992. "Combustion instability related to vortex shedding in dump combustors and their passive control". *Progress in Energy and Combustion Science,* ***18***(2), pp. 117–132.

[4] Lieuwen, T. C., and Yang, V., 2005. *Combustion instabilities in gas turbine engines: operational experience, fundamental mechanisms, and modeling*. American Institute of Aeronautics and Astronautics.

[5] Prasad, A., and Williamson, C. H., 1997. "The instability of the shear layer separating from a bluff body". *Journal of Fluid Mechanics,* ***333***, pp. 375–402.

[6] Provansal, M., Mathis, C., and Boyer, L., 1987. "Bénard-von kármán instability: transient and forced regimes". *Journal of Fluid Mechanics,* ***182***, pp. 1–22.

[7] Griffin, O., and Hall, M., 1991. "Vortex shedding lock-on and flow control in bluff body wakes". *Journal of Fluids Engineering,* ***113***(4), pp. 526–537.

[8] Yu, M.-H., and Monkewitz, P. A., 1990. "The effect of nonuniform density on the absolute instability of two-dimensional inertial jets and wakes". *Physics of Fluids A: Fluid Dynamics,* ***2***(7), pp. 1175–1181.

[9] Emerson, B., O'Connor, J., Juniper, M., and Lieuwen, T., 2012. "Density ratio effects on reacting bluff-body flow field characteristics". *Journal of Fluid Mechanics,* ***706***, pp. 219–250.

[10] Erickson, R., and Soteriou, M., 2011. "The influence of reactant temperature on the dynamics of bluff body stabilized premixed flames". *Combustion and Flame,* ***158***(12), pp. 2441–2457.

[11] Emerson, B. L., Noble, D. R., and Lieuwen, T. C., 2014. "Stability analysis of reacting wakes: The physical role of flame-shear layer offset". In 52nd Aerospace Sciences Meeting.

[12] Shanbhogue, S., Shin, D.-H., Hemchandra, S., Plaks, D., and Lieuwen, T., 2009. "Flame-sheet dynamics of bluff-body stabilized flames during longitudinal acoustic forcing". *Proceedings of the Combustion Institute,* ***32***(2), pp. 1787–1794.

[13] Emerson, B., and Lieuwen, T., 2015. "Dynamics of harmonically excited, reacting bluff body wakes near the global hydrodynamic stability boundary". *Journal of Fluid Mechanics,* ***779***, pp. 716–750.

[14] Preetham, Santosh, H., and Lieuwen, T., 2008. "Dynamics of laminar premixed flames forced by harmonic velocity disturbances". *Journal of Propulsion and Power,* ***24***(6), pp. 1390–1402.

[15] Humphrey, L. J., Emerson, B., and Lieuwen, T. C., 2018. "Premixed turbulent flame speed in an oscillating disturbance field". *Journal of Fluid Mechanics,* ***835***, pp. 102–130.

[16] Hirsch, C., Fanaca, D., Reddy, P., Polifke, W., and Sattelmayer, T., 2005. "Influence of the swirler design on the flame transfer function of premixed flames". In Turbo Expo: Power for Land, Sea, and Air.

[17] Palies, P., Durox, D., Schuller, T., and Candel, S., 2010. "The combined dynamics of swirler and turbulent premixed swirling flames". *Combustion and Flame,* ***157***(9), pp. 1698–1717.

[18] Kim, K. T., and Santavicca, D. A., 2013. "Interference mechanisms of acoustic/convective disturbances in a swirl-stabilized lean-premixed combustor". *Combustion and Flame,* ***160***(8), pp. 1441–1457.

[19] Æsøy, E., Nygård, H. T., Worth, N. A., and Dawson, J. R., 2022. "Tailoring the gain and phase of the flame transfer function through targeted convective-acoustic interference". *Combustion and Flame,* ***236***, p. 111813.

[20] Hemchandra, S., and Lieuwen, T., 2010. "Local consumption speed of turbulent premixed flames–an analysis of "memory effects"". *Combustion and Flame,* ***157***(5), pp. 955–965.

[21] Hemchandra, S., Peters, N., and Lieuwen, T., 2011. "Heat release response of acoustically forced turbulent premixed flames—role of kinematic restoration". *Proceedings of the Combustion Institute,* ***33***(1), pp. 1609–1617.

[22] Chaparro, A., Landry, E., and Cetegen, B. M., 2006. "Transfer function characteristics of bluff-body stabilized, conical v-shaped premixed turbulent propane–air flames". *Combustion and Flame,* ***145***(1-2), pp. 290–299.

[23] Kheirkhah, S., and Gülder, Ö., 2014. "Topology and brush thickness of turbulent premixed v-shaped flames". *Flow, Turbulence, and Combustion,* ***93***(3), pp. 439–459.

[24] Tyagi, A., Boxx, I. G., Peluso, S., and O'Connor, J. A., 2019. "Statistics of local flame-flame interactions in flame interaction zones of two v-flames". In AIAA Scitech 2019 Forum.

[25] Karmarkar, A., Tyagi, A., Hemchandra, S., and O'Connor, J., 2021. "Impact of turbulence on the coherent flame dynamics in a bluff-body stabilized flame". *Proceedings of the Combustion Institute,* ***38***(2), pp. 3067–3075.

[26] Balachandran, R., Dowling, A., and Mastorakos, E., 2008. "Non-linear response of turbulent premixed flames to imposed inlet velocity oscillations of two frequencies". *Flow, Turbulence, and Combustion,* ***80***, pp. 455–487.

[27] Kim, K. T., Lee, J. G., Quay, B., and Santavicca, D., 2010. "Response of partially premixed flames to acoustic velocity and equivalence ratio perturbations". *Combustion and Flame,* ***157***(9), pp. 1731–1744.

[28] Hussain, A. F., 1983. "Coherent structures—reality and myth". *Physics of Fluids,* ***26***(10), pp. 2816–2850.

[29] Tyagi, A., Boxx, I., Peluso, S., and O'Connor, J., 2019. "Statistics and topology of local flame–flame interactions in turbulent flames". *Combustion and Flame,* ***203***, pp. 92–104.

[30] Karmarkar, A., and O'Connor, J., 2022. "Interaction between coherent and turbulent oscillations in non-reacting and reacting wake flows". *Journal of Fluid Mechanics,* ***accepted***.

[31] Karmarkar, A., and O'Connor, J., 2022. "Impact of turbulence on flame brush development of acoustically excited rod-stabilized flames". *Proceedings of the Combustion Institute,* ***in press***.

[32] Khabbouchi, I., Fellouah, H., Ferchichi, M., and Guellouz, M. S., 2014. "Effects of free-stream turbulence and reynolds number on the separated shear layer from a circular cylinder". *Journal of Wind Engineering and Industrial Aerodynamics,* ***135***, pp. 46–56.

[33] Shanbhogue, S. J., Seelhorst, M., and Lieuwen, T., 2009. "Vortex phase-jitter in acoustically excited bluff body flames". *International Journal of Spray and Combustion Dynamics,* ***1***(3), pp. 365–387.

[34] Williamson, C. H., 1996. "Vortex dynamics in the cylinder wake". *Annual Review of Fluid Mechanics,* ***28***(1), pp. 477–539.

[35] Boyer, L., and Quinard, J., 1990. "On the dynamics of anchored flames". *Combustion and Flame,* ***82***(1), pp. 51–65.